***Conference on Modelling Fluid Flow (CMFF'25)***
***The 19th International Conference on Fluid Flow Technologies***
***Budapest, Hungary, August 26 - August 29, 2025***

# A COMPREHENSIVE ANALYSIS OF VARIABLE INLET GUIDE VANE ON CAVITATION AND HYDRAULIC PERFORMANCE OF AN AXIAL-FLOW PUMP

Duc-Anh NGUYEN[1,2], Jin-Hyuk KIM[1,2*]

[1] Convergence Manufacturing System Engineering (Green Process and Energy System Engineering), University of Science & Technology, Daejeon, 34113, South Korea
[2] Carbon Neutral Technology R&D Department, Korea Institute of Industrial Technology, Cheonan, 31056, South Korea
* Correspondence author: Jin-Hyuk Kim (Ph.D.) E-mail: jinhyuk@kitech.re.kr

## ABSTRACT

Addressing cavitation in axial-flow pumps is crucial for enhancing efficiency, reducing vibration, and extending pump lifespan. Therefore, this study proposes a novel approach to increase hydraulic performance and mitigate cavitation at different flow rates by altering the flow direction into the impeller using variable inlet guide vanes (IGV). To analyze the internal flow characteristic, this study employed numerical simulations, utilizing the Reynolds-averaged Navier-Stokes equations in conjunction with a shear stress transport turbulence model. The experiments were performed to validate the accuracy of the numerical results. The results show that changes in efficiency are less pronounced when adjusting the IGV setting angle from negative to positive, whereas the total head consistently increases by an average of 8.06% at the best efficiency point. The formation of the tip leakage vortex within the axial-flow pump at the deep stall point is attributed to the combination of tip leakage flow and flow separation at the leading edge of the impeller. Although negative IGV setting angles can degrade the hydraulic performance at the best efficiency point (BEP) and overload conditions, they also significantly reduce cavitation, reaching up to 86.253% at the BEP. At part-load conditions, positive IGV setting angles effectively reduce cavitation, especially at the deep stall condition with a reduction of up to 40.64%.

**Keywords: Axial-flow pump, variable inlet guide vane, impeller, computational fluid dynamics, hydraulic performance, cavitation.**

## NOMENCLATURE

| | | |
|---|---|---|
| $g$ | $[m/s^2]$ | Gravitational acceleration |
| $H$ | $[m]$ | Total head coefficient |
| $\psi$ | [-] | Total head |
| $D$ | $[m]$ | Impeller diameter |
| $Q$ | [-] | Flow rate coefficient |
| $\varphi$ | $[m/s]$ | Flow rate |
| $\varphi_d$ | $[m/s]$ | Flow rate at the BEP |
| $n$ | $[rpm]$ | Rotating speed |
| $\lambda$ | [-] | Specific speed |
| $\eta$ | [%] | Efficiency |

**Subscripts and Superscripts**

| | |
|---|---|
| IGV | Inlet guide vane |
| DV | Diffuser vane |
| LE | Leading edge |
| TE | Trailing edge |
| SS | Suction side |
| PS | Pressure side |
| TLV | Tip leakage vortex |
| BEP | Best efficiency point |
| GCI | Grid convergence index |

## 1. INTRODUCTION

A pump, a device that moves fluids from one place to another, is an indispensable device in daily life. Pumps are used in a variety of applications, including water distribution, sewage treatment, and industrial processes. In addition, the pump is a device that consumes a lot of energy and can cause noise pollution. Research by Capurso et al. [1] indicated that the power usage of centrifugal pumps in Europe amounts to 120 TWh/day, which corresponds to an average carbon generation of 475 gCO2/kWh. A mere 1% enhancement in energy performance can lead to a reduction of at least 570 tCO2/day in greenhouse gas emissions. Therefore, optimizing and improving the performance of the pump is an important factor in saving energy and protecting the environment, particularly for axial-flow pumps, which are large, energy-intensive devices.

Compared to other types of pumps, an axial-flow pump is capable of generating the largest flow rate at high performance and is extensively utilized in water systems, agricultural applications, draining in industrial and city settings. The flow characteristic within an axial-flow pump is characterized by chaos, turbulent and unsteady dynamics, often resulting in the formation of various vortices, including tip leakage vortex (TLV) [2-4], separation flow [5], horseshoe vortex [6], and corner vortex [5, 6]. Additionally, hydraulic losses caused by cavitation and leakage flow at the impeller gap can induce strong vibrations, generate excessive noise, and damage the impeller blades. Therefore, not only the axial-flow pump but all types of pumps, increasing performance, reducing cavitation are important factors in stable and safe pump operation.

Cavitation [7] is an undesirable phenomenon that can cause significant wear and tear on the metal blades of pumps [8, 9], turbines [10-11], and propellers [12]. It reduces operational efficiency, causes unpleasant vibrations, leads to high energy consumption, system instability, and diminished pump component lifespan. According to Orlandi et al. [13], cavitation occurs when the pressure of a liquid drops below its saturation vapor pressure, leading to the formation of gas bubbles. As these bubbles move into regions of higher pressure, they implode, creating powerful shock waves that can damage the blade surface. The repeated implosion of gas bubbles can severely erode the metal surface, especially on the impeller. Zhang et al. [14] noted that cavitation at the tip region of the axial-flow pump varied over time and encompassed several types at tip clearance, in TLV, on the suction side (SS), and at the trailing edge (TE). In the study of Zhang et al. [15], cavitation intensity in axial-flow pumps also changed with flow rate conditions and was categorized into different stages, including non-cavitating, incipient cavitation, critical cavitation, and deep cavitation. Due to its damaging effects, detection and elimination of cavitation are key considerations in pump design.

To enhance the hydraulic performance and reduce vibration in axial-flow pumps, variable IGV is currently being considered as a potential solution [16-19]. However, existing research has not yet demonstrated the effect of variable IGV on the reduction of cavitation. Consequently, this study is performed to comprehensively examine the cavitation phenomenon in axial-flow pumps through both numerical simulations and experimental investigations. In addition, this study proposes a novel approach to mitigate cavitation by altering the flow direction into the impeller using a variable IGV. By changing the flow direction, it is anticipated that flow separation within the impeller will be reduced, leakage flow minimized, and overall cavitation and pump performance significantly improved. Cavitation changes in the axial-flow pump will be carefully analyzed via cavitation visualization and the determination of cavitation volume.

## 2. METHODOLOGY

### 2.1. Axial-flow pump model

The axial-pump model utilized in this study consists of four IGVs, four impellers, and seven diffuser vanes (DV) as demonstrated in figure 1(a). The pump is designed to operate at a specific speed of 1204 and the rotating speed coefficient of 0.7893 as calculated according to Eq. (1) and Eq. (2), respectively. At the best efficiency point (BEP), the design head and design flow rate coefficient are 1.584 and 0.4319 as calculated according to Eq. (3) and Eq. (4), respectively.

$$\lambda = n[rpm]\frac{\varphi^{0.5}\,[\frac{m^3}{min}]}{\psi^{0.75}\,[m]} \tag{1}$$

$$\chi = \frac{nD}{\sqrt{g\psi}} \tag{2}$$

$$H = \frac{g\psi}{n^2D^2} \tag{3}$$

$$Q = \frac{\varphi}{nD^3} \tag{4}$$

where $n$, $\varphi$, $\psi$, $D$, and $g$ denote the rotational speed, flow rate, total head, impeller diameter, and acceleration of gravity, respectively.

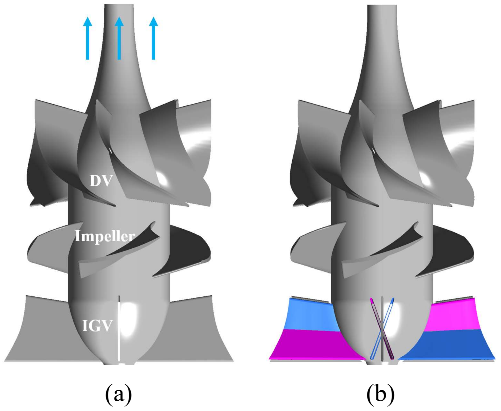

(a) (b)

**Figure 1. Axial-flow pump configuration. (a) Original design, (b) New design with variable IGV (green: $20°$, pink: $-20°$)**

The axial-flow pump was tested at the Korea Institute of Machinery & Materials with the IGV chamber made transparent to easily see the formation and evolution of cavitation during operation with the help of a high-speed camera and fill light. The NX4-S1 camera model from Integrated Design Tools incorporation was synchronized with the computer system. In addition, to achieve the efficiency and power consumption of the pump, a series of modern measuring devices such as digital pressure gauge, magnetic flow meter, and power meter were used, as can be seen in figure 2. Accuracy of measuring device is presented in Table 1 and detailed information about the experimental system can be found in previous studies [6, 20].

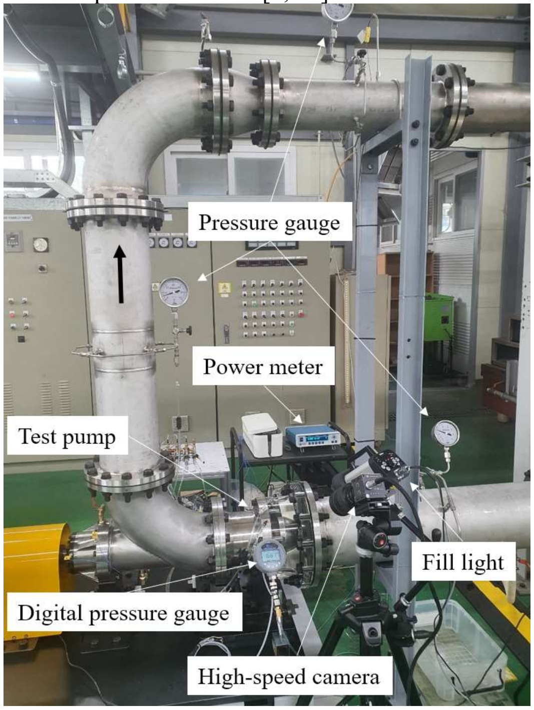

**Figure 2. Measuring instruments in the pump test [20]**

**Table 1. Accuracy of measuring equipment [6]**

| Equipment | Operational range | Uncertainty |
|---|---|---|
| Absolute pressure transducer | 0−200 (kPa) | ± 0.25% |
| Differential pressure transducer | 0−500 (kPa) | ± 0.2% |
| Torque measurement | 0−200 (Nm) | ± 0.2% |
| Rotating measurement | 0−20,000 (rpm) | ± 0.02% |
| Flowmeter | 0−900 ($m^3$/hr) | ± 0.2% |

## *2.2. Numerical method*

Figure 3 shows the grid system for the numerical simulation with a hexahedral grid structure. The grid system is refined at wall surfaces with multiple layers of small meshes to ensure that the averaged $y^+$ value is less than two. The grid growth rate was maintained below 1.3. The grid independence is checked by utilizing the Grid Convergence Index (GCI) [21] based on three different grid systems ($N_1$, $N_2$, and $N_3$) with a grid refinement ratio of larger than 1.3. The values of the key parameter (efficiency) are normalized according to the efficiency value of the $N_1$ grid system with only impeller in the computational model. As can be seen in Table 2, the $GCI_{fine}^{21}$ values and extrapolated relative error values ($e_{ext}^{21}$) are small enough [21] to confirm the convergence of the grid system. Therefore, the optimal grid system in this study consists of 0.55 × $10^6$, 0.67 × $10^6$, and 0.57 × $10^6$ nodes for one IGV, impeller, and DV passages, respectively.

In the numerical simulation, the boundary conditions of the axial-flow pump are established based on ANSYS CFX-Pre with the fluids including water and water vapor at 25°. The inlet and outlet of the computational domain are respectively set as total pressure and mass flow rate. The blade, hub, and shroud surfaces are set as non-slip walls. The interfaces between the stationary and rotating domains are set as the mixing-plane. Rayleigh Plesset is selected as the cavitation model with a saturation pressure of 3170 Pa and the initial average bubble diameter of $2 \times 10^{-6}\, m$. The shear stress transport [22] coupled with the reattachment modification option is used as an optimum turbulence model to be able to accurately predict cavitation, vortex flow, and separation flow in this study.

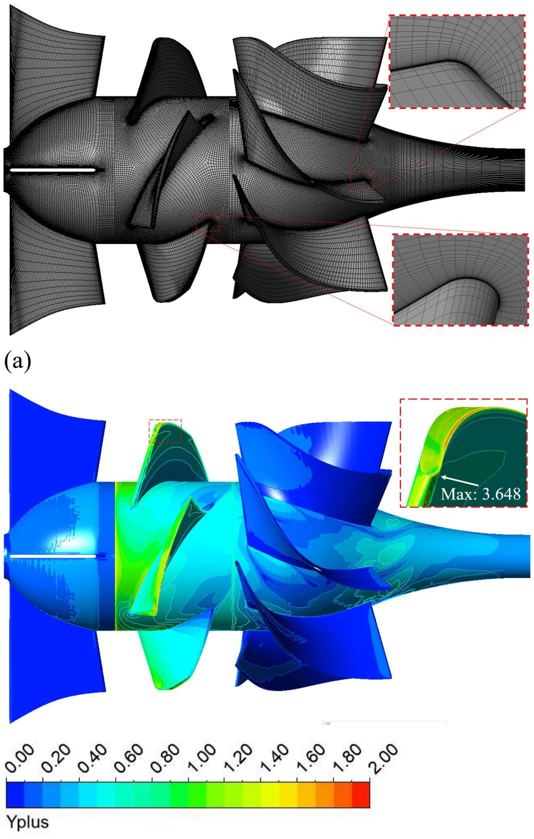

(a)

(b)

**Figure 3. The established grid for numerical simulation. (a) grid system, (b) y+ distribution.**

**Table 2. Grid sensitivity analysis [6]**

| | Only impeller (No. of nodes in impeller) | IGV and impeller (No. of nodes in IGV) | Full component (No. of nodes in DV) |
|---|---|---|---|
| $N_1$ | 666,773 | 550,272 | 571,540 |
| $N_2$ | 265,681 | 248,100 | 256,250 |
| $N_3$ | 115,260 | 409,164 | 114,500 |
| $r_{21}$ | 1.359 | 1.304 | 1.307 |
| $r_{32}$ | 1.321 | 1.315 | 1.308 |
| $\eta_1/\eta_1$ | 1.000 | 0.976 | 1.043 |
| $\eta_2/\eta_1$ | 0.993 | 0.975 | 1.042 |
| $\eta_3/\eta_1$ | 0.972 | 0.957 | 1.026 |
| $e_{ext}^{21}$ | 0.00325 | 0.00014 | 0.00012 |
| $\mathrm{GCI}_{\mathrm{fine}}^{21}$ | 0.00407 | 0.00017 | 0.00016 |

## 3. RESULTS AND DISCUSSIONS

### *3.1. Validation*

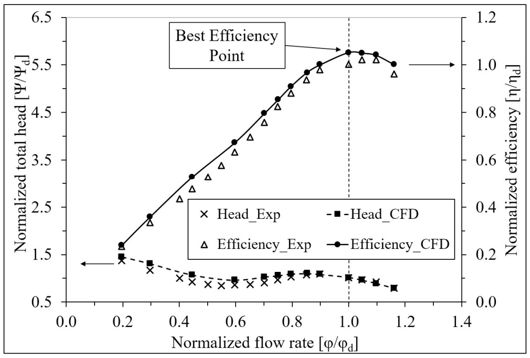

**Figure 4. The hydraulic performance curves in simulation and in experiment**

Figure 4 compares the efficiency and total head of the axial-flow pump measured in the experiment and in the numerical calculation. The efficiency and total head values are normalized using their values at the BEP of the experimental results. As can be seen in figure 4, the numerical results are consistent with the experimental data. The discrepancy between the numerical and experimental data is about 5.2% for efficiency and 1.256% for total head at the BEP. The relatively large difference in efficiency at the BEP is caused by the instability of the flow field in the experiment at a high flow rate due to the absence of a booster pump. For this reason, the experimental data at overload conditions are not available. In addition, errors in the measuring equipment and extrapolation errors in numerical calculations are also the causes of these differences.

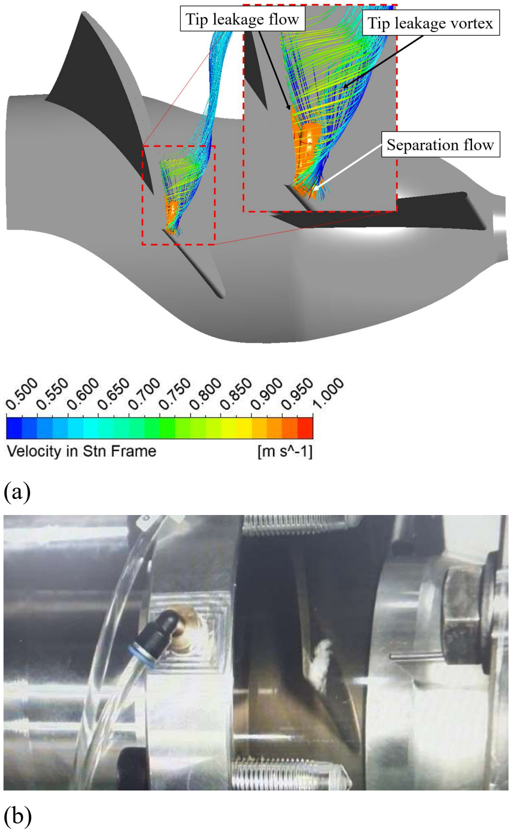

(a)

(b)

**Figure 5. Cavitation visualization. (a) in simulation (orange: vapor volume fraction of 0.94), (b) in experiment.**

To further confirm the accuracy of the numerical results, cavitation visualization is extracted and compared with the experimental result at the deep stall point ($0.6\varphi_d$) as shown in figure 5. The numerical simulation predicts well the cavitation bubbles formed at the leading edge (LE) of the impeller. Based on the simulation results, cavitation formation is based on two main factors including tip leakage flow and separation flow. The combination of these two flows created a TLV that separates from the impeller surface. With high rolling velocity mainly caused by the tip leakage flow, a large void with low pressure inside the TLV is formed. The pressure inside this void drops below the saturation vapor pressure, ultimately leading to the formation of cavitation bubbles.

### *3.2. Hydraulic performance*

Figure 6 presents the total head and efficiency curves across various IGV angles. The total head and efficiency values are normalized to their respective values at the BEP of the 0° IGV angle model, which serves as the reference model. When varying the IGV angle, changes in efficiency are less pronounced, particularly in the low-flow rate region, compared to the more significant variations observed in the total head. The minimal changes in efficiency can be attributed to the turbulence within the flow field, which elevates the load on the impeller and subsequently increases power consumption. As a result, the efficiency of the reference model remains superior to that of other IGV setting angles, except at high flow rates where a favorable match between the flow and impeller blade angle can occur. Around the BEP, the efficiency for too large and too low IGV angles is significantly lower in comparison to the reference model, with the efficiencies at 20° and −20° IGV under the BEP being reduced by 2.29% and 1.82%, respectively.

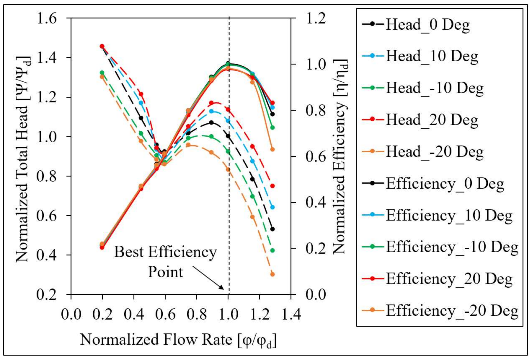

**Figure 6. The hydraulic performance at different IGV setting angle**

The head of the axial-flow pump progressively rises as the IGV angle transitions from negative to positive, exhibiting an average increase of 8.06% at the BEP. This enhancement is primarily due to the role of IGV in facilitating flow into the impeller; as the IGV angle rises, the absolute velocity of the flow entering the impeller becomes increasingly compatible with the relative velocity. This alignment results in elevated velocity and pressure in the flow exiting the impeller. In addition, the saddle zone also becomes more prominent as the IGV angle rises, owing to significant losses in both IGV and impeller passages at high IGV angles. These high angles also increase the incident angle at LE of the impeller, promoting the flow separation on the SS of the impeller compared to the reference model, particularly under low flow rate conditions. Based on the hydraulic performance curves, it can be seen that at the same head, the axial-flow pump can operate at various flow rates to achieve optimal performance depending on the variable IGV.

### *3.3. Internal flow characteristics*

To clearly observe the impact of variable IGV on cavitation within the impeller, figure 7 depicts cavitation represented by an orange iso-vapor volume fraction of 0.5 across −10°, 0°, and 10° IGV setting angle models at different flow rates. Intense cavitation is observed at the LE of the impeller for all three models at the deep stall point. Although the cavitation of the 10° model is smaller than in the other two models, this difference does not seem to be significant as observed in figure 7(a). However, the bubble volume of the 10° model is reduced by 40.64% and 16.38% compared to the reference model and −10° model as presented in the figure 8. Figure 7 also shows the turbulence kinetic energy (TKE) distribution at different cross-sections to evaluate the energy loss caused by TLV and cavitation. It can be stated that the TKE generated at the deep stall point is the largest among all three IGV models due to the chaotic flow characteristics and the presence of strong cavitation. While the 10° model reduces cavitation, it leads to a 13.51% increase in TKE compared to the reference model, whereas the −10° model yields a 10.68% reduction in TKE.

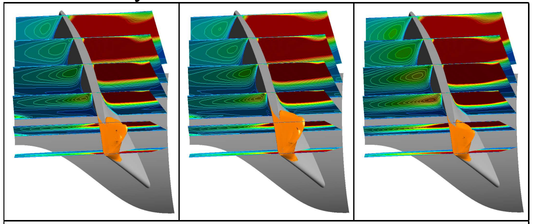

(a) At the deep stall point ($0.6\varphi_d$)

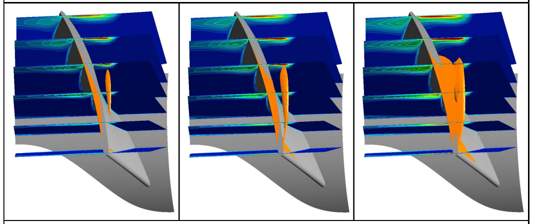

(b) At the BEP ($1.0\varphi_d$)

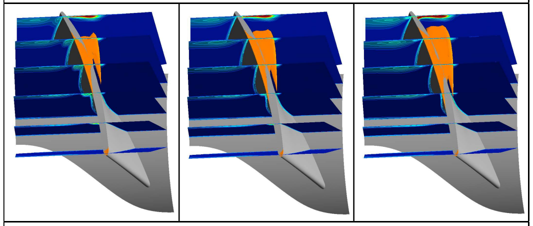

(c) At overload condition ($1.28\varphi_d$)

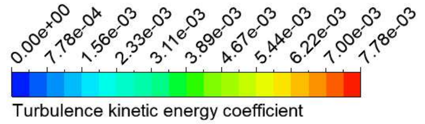

**Figure 7. Cavitation in the impeller at different flow rate conditions (left: −10°; middle: 0°; right: 10°)**

The difference in cavitation is most apparent at the BEP, as shown in figure 7(b). In all three models, cavitation is markedly reduced in the −10° model, with cavitation streaks nearly disappearing at the LE of the impeller. Furthermore, cavitation induced by leakage flow at the gap and TLV is significantly diminished compared to the reference model. Therefore, the turbulence kinetic energy and bubble volume of the −10° model decreased by up to 19.643% and 86.253%, respectively in comparison with the reference model. While increasing the IGV setting angle may enhance the total head, it also increases the risk of severe cavitation formation and the TKE at the BEP, as demonstrated in figure 7(b, right). The closeness of absolute velocity to relative velocity not only intensifies leakage flow through the gap but also generates a substantial pressure differential, leading to a marked pressure drop on the SS, as can be seen in figure 9(b), thereby fostering conditions favorable for cavitation.

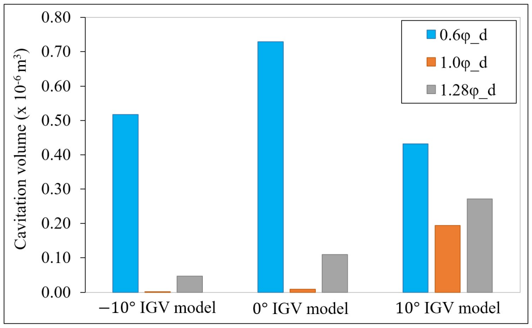

**Figure 8. The volume of cavitation in different conditions**

Likewise, under overload conditions, cavitation manifests more robustly at positive IGV angles, whereas it diminishes at negative angles when compared to the reference model. Therefore, the bubble volume of the 10° model at the BEP and $1.28\varphi_d$ increased by 20.77 times and 2.47 times compared to the reference model, respectively. Correspondingly, the TKE of the 10° model increased by 39.78% at the BEP and 19.63% at $1.28\varphi_d$ in comparison to the reference model. It should be noted that while the TKE of the 10° model exhibits an increase in comparison with the reference model, the hydraulic performance is also enhanced, especially at overload conditions. This is attributed to the improved compatibility between the flow angle and blade angle at the LE of the impeller, which consequently results in an increase of the velocity and energy within the impeller domain, thereby contributing to both the elevated TKE and the hydraulic performance observed in the10° model.

The cavitation visualization indicates a tendency for cavitation to gradually migrate from the LE to the TE of the impeller as the flow rate increases. Additionally, analysis of the bubble volume in figure 8 reveals that the negative IGV angles are more effective than positive angles in mitigating cavitation within the impeller, particularly around the BEP and under overload conditions.

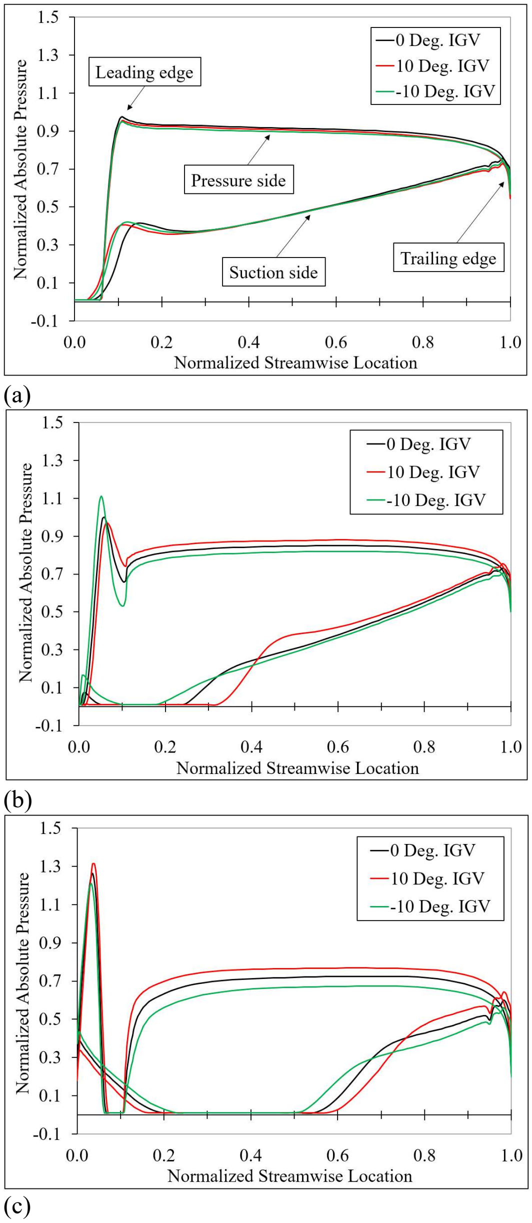

(a)

(b)

(c)

**Figure 9. The pressure distribution at 95% span of the impeller. (a) at the $0.6\varphi_d$, (b) at the BEP ($\varphi_d$), (c) at the $1.28\varphi_d$**

Figure 9 shows the absolute pressure distribution at 95% span where cavitation occurs prominently for −10°, 0°, and 10° IGV angle models across various flow rates. The pressure values are normalized to the maximum pressure of the reference model at the BEP. At the deep stall point, a significant pressure drop is observed at the LE of the impeller, which facilitates the formation and development of cavitation, as illustrated in figure 7(a). The pronounced differences in pressure distribution among the different models are mainly at the BEP and $1.28\varphi_d$ contributing to noticeable variations in the total head curves, as shown in figure 6. However, the pressure drop at the SS of these flow conditions continues to promote cavitation formation, particularly at the 10° model. At the BEP, the pressure drop extends to a streamwise location of 0.3, resulting in the appearance of elongated cavitation streaks, as depicted in figure 7(b). For the 10° model, while the pressure on the pressure side (PS) is the highest, the pressure drop at the SS is also the most significant, leading to substantial cavitation within the impeller domain. At the $1.28\varphi_d$, the pressure distribution around the LE becomes highly complex, characterized by a peak pressure due to the stagnation point, alongside sharp pressure drops resulting from velocity acceleration on both sides of the impeller. The majority of cavitation observed in figure 7(c) is a consequence of the abrupt pressure drop within the TLV between streamwise positions 0.2 and 0.6. Additionally, the irregular pressure distribution at the TE is also clearly visible in figure 9, attributed to the presence of the TE vortex [23].

To evaluate the energy loss in the axial-flow pump, the distribution of TKE at 95% span is presented in figure 10 for the three IGV models at different flow rate conditions. The TKE value is normalized by the square of the maximum velocity at the impeller tip. It is evident that operation at the deep stall point results in the highest energy loss among the three operational conditions due to the complexity of the flow. A significant amount of loss occurs around the LE of the impeller at the SS and subsequently spreads throughout the impeller passage. Furthermore, the turbulence also affects the IGV, leading to considerable energy loss at the outlet of the IGV. The changes in hydraulic performance at the deep stall point are primarily reflected in the energy loss observed at the outlet of the IGV and the TE of the DV. At the BEP and $1.28\varphi_d$, energy loss is improved markedly compared to that at the deep stall point. However, the presence of cavitation and TLV still results in considerable energy loss within the impeller domain, as clearly illustrated in figures 10(b, right) and 10(c).

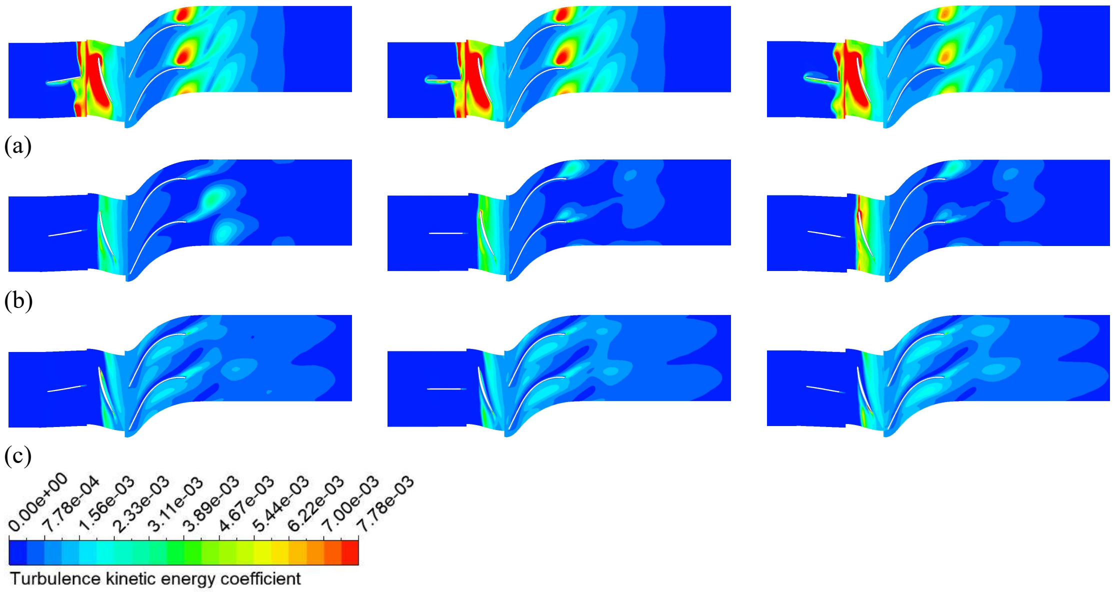

**Figure 10. The turbulence kinetic energy distribution at 95% span(left: $-10°$; middle: $0°$; right: $10°$). (a) at $0.6\varphi_d$, (b)at the BEP ($\varphi_d$), (c) at $1.28\varphi_d$**

## 4. CONCLUSIONS

This study investigates the influence of variable IGV on the hydraulic performance and cavitation of the axial-flow pump, utilizing five IGV setting angles, including 0°, ±10°, and ±20°. To validate the numerical simulation results, hydraulic performance curves and cavitation visualizations are compared against experimental data. The key findings derived from the numerical simulations are drawn as follows:

A. The variable IGV does not significantly alter the efficiency of the axial-flow pump, except under high flow rate conditions. However, increasing the IGV angle leads to a substantial increase in the total head with an average increase of around 8.06% and makes the saddle zone more pronounced. Therefore, variable IGV is particularly advantageous for optimizing the efficiency of axial-flow pumps by operating at different flow rates while maintaining the desired head.

B. Cavitation at the deep stall point is primarily attributed to the pressure drop within the TLV, resulting from a combination of tip leakage flow and separation flow at the LE of the impeller. At the deep stall point, while the 10° model achieves a 40.64% reduction in cavitation, it concurrently results in a 13.51% increase in TKE whereas the $-10°$ model demonstrates a 10.68% reduction in TKE compared to the reference model. Under operating conditions around the BEP and under overload conditions, positive IGV angles increase total head, while negative angles mitigate cavitation by up to 86.253% in comparison with the reference model. Furthermore, the study further demonstrates a correlation between flow rate and cavitation location, with higher flow rates resulting in cavitation occurring closer to the TE of the impeller.

It should be noted that the hydraulic performance and cavitation characteristics may vary depending on different pump models. This study has not considered the time-dependent evolution of cavitation through unsteady-state simulations. In the future, the Large Eddy Simulation with the Wall-Adapting Local Eddy-viscosity subgrid-scale model will be employed to observe and thoroughly analyze cavitation behavior and internal flow characteristics of the axial-flow pump at various stages across different IGV setting angles.

## ACKNOWLEDGEMENTS

This work was supported by Korea Institute of Energy Technology Evaluation and Planning (KETEP) grant funded by the Korea government (MOTIE) (2021202080026A, Development of Variable Operating Technology for Medium and Large Size Pump) and partially was supported by UST Young Scientist+ Research Program 2024 through the University of Science and Technology. (No. 2024YS21).

## REFERENCES

1. Capurso, T., Bergamini, L., Torresi, M., 2022, "A new generation of centrifugal pumps for high conversion efficiency," *Energy Convers Manage*, Vol. 256, 115341.
2. Zhang, D., Shi, L., Shi, W., Zhao, R., Wang, H., Esch, B. P. M. V., 2015, "Numerical analysis of unsteady tip leakage vortex cavitation cloud and unstable suction-side-perpendicular cavitating vortices in an axial flow pump", *Int J Multiphase Flow*, Vol. 77, pp. 244-259.
3. Shen, X., Zhang, D., Xu, B., Shi, W., Esch, B. P. M. V., 2021, "Experimental and numerical investigation on the effect of tip leakage vortex induced cavitating flow on pressure fluctuation in an axial flow pump", *Renew Energy*, Vol. 163, pp. 1195-1209.
4. Shen, X., Zhao, X., Xu, B., Zhang, D., Yang, G., Shi, W., Esch, B. P. M. V., 2022, "Unsteady characteristics of tip leakage vortex structure and dynamics in an axial flow pump", *Ocean Eng*, Vol. 266, pp. 1-18.
5. Wang, C., Wang, F., Xie, L., Wang, B., Yao, Z., Xiao, R., 2021, "On the vortical characteristics of horn-like vortices in stator corner separation flow in an axial flow pump", *ASME J Fluids Eng*, Vol. 143, 061201.
6. Nguyen, D. A., Lee, H. J., Kim, S., Choi, B. L., Choi, D. H., Kim, G. S., Sun, S., Kim, J. H., 2024, "Multiobjective hydraulic optimization of the diffuser vane in an axial flow pump", *Phys Fluids*, Vol. 36, pp. 1-25.
7. Kan, K., Binama, M., Chen, H., Zheng, Y., Zhou, D., Su, W., Muhirwa, A., 2022, "Pump as turbine cavitation performance for both conventional and reverse operating modes: A review", *Renew Sustain Energy Rev*, Vol. 168, pp. 1-21.
8. Gong, J., Luo, W. Z., Wu, T. C., Zhang, Z. Y., 2022, "Numerical analysis of vortex and cavitation dynamics of an axial-flow pump", *Eng Appl Comput Fluid Mech*, Vol. 16, pp. 1921-1938.
9. Jia, X. Q., Zhang, Y., Lv, H., Zhu, Z. C., 2023, "Study on external performance and internal flow characteristics in a centrifugal pump under different degrees of cavitation", *Phys Fluids*, Vol. 35, 014104.
10. Shahzer, M. A., Kim, J. H., 2024, "Investigation of role of fins in a francis turbine model's cavitation-induced instabilities under design and off-design conditions", *Energy*, Vol. 292, pp. 1-17.
11. Shamsuddeen, M. M., Park, J. W., Choi Y. S., Kim, J. H., 2020, "Unsteady multi-phase cavitation analysis on the effect of anti-cavity fin installed on a kaplan turbine runner", *Renew Energy*, Vol. 162, pp. 861-876.
12. Tan, Q., Ding, Y., Sui, C., Xiang, L., 2024, "Effects of propeller cavitation on ship propulsion performance in off-design operating conditions", *Ocean Eng*, Vol. 313, pp. 1-16.
13. Orlandi, F., Montorsi, L., Milani, M., 2023, "Cavitation analysis through CFD in industrial pumps: A review", *Int J Thermofluids*, Vol. 20, pp. 1-26.
14. Zhang, D., Shi, L., Zhao, R., Shi, W., Pan, Q., Esch, B. P. M. V., 2017, "Study on unsteady tip leakage vortex cavitation in an axial-flow pump using an improved filter-based model", *J Mech Sci Tech*, Vol. 31, pp. 659–667.

15. Zhang, R., Chen, H. X., 2013, “Numerical analysis of cavitation within slanted axial-flow pump”, *J Hydrodyn*, Vol. 25, pp. 663-672.

16. Yang, F., Hu, W. Z., Li, C., Liu, C., Jin, Y., 2020, “Computational study on the performance improvement of axial-flow pump by inlet guide vanes at part loads”, *J Mech Sci Technol*, Vol. 34, pp. 4905-4915.

17. Zhang, W. P., Shi, L. J., Tang, F. P., Duan, X. H., Liu, H. Y., Sun, Z. Z., 2020, “Analysis of inlet flow passage conditions and their influence on the performance of an axial-flow pump”, *J Power Energy*, Vol. 0, pp. 1-14.

18. Nguyen, D. A., Kim, J. H., 2024, “Co-adjustable guide vane and diffuser vane to improve the energy generation potential of an axial-flow pump as turbine”, *Energy*, Vol. 291, pp. 1-15.

19. Shi. L. J., Chi, Y., Wang, L., Xu, T., Jiang, Y. H., Xing, J., Yan, B. Y., Chen, Y. Y., Han, Y., 2023, “Numerical simulation and model test of the influence of guide vane angle on the performance of axial flow pump”, *Phys Fluids*, Vol. 35, 015129.

20. Nguyen, D. A., Dinh, C. T., Kim, J. H., 2024, “Improvement in energy performance from the construction of inlet guide vane and diffuser vane geometries in an axial-flow pump”, *Sci Rep*, Vol. 14, pp. 1-27.

21. Celik, I. B., 2008, "Procedure for estimation and reporting of uncertainty due to discretization in CFD applications", *J Fluid Eng*, Vol. 130, pp. 1-4.

22. Menter, F. R., 1994, “Two-equation eddy-viscosity turbulence models for engineering applications”, *AIAA J*, Vol. 32, pp. 1598–1605.

23. Zierke, W. C., Straka, W. A., 1996, “Flow visualization and the three-dimensional flow in an axial-flow pump”, J Propul Power, Vol. 12, pp. 250–259.